Chapter 13

Reduced-order Observer Analysis in MBPC Techniques Applied to the Six-phase Induction Motor Drives

Raúl Gregor, Jorge Rodas, Derlis Gregor and Federico Barrero

Additional information is available at the end of the chapter

Abstract

Model-based predictive control techniques have been recently applied with success in power electronics, particularly in the fields of current control applied to AC multiphase electrical drives. In AC electrical drives control, most of state variables (i.e., rotor currents, rotor fluxes, etc.) cannot be measured, so they must be estimated. As a result of this issue, this chapter proposes a comparative study of reduced-order observers used to estimate the rotor currents in an model-based predictive current control applied to the six-phase induction motor. The proposed control techniques are evaluated using the Luenberger observer and the optimal estimator based on Kalman filter. Different operation modes are analyzed and are further compared in terms of statistical parameters of performance (i.e., covariance, standard deviation, mean square error, etc.). The effectiveness of proposed methods is verified by a set of comparative experiments obtained by using a six-phase induction motor system experimental setup.

Keywords: Model-based predictive control (MBPC), Kalman filter (KF), Luenberger observer (LO), Six-phase induction motor (SpIM)

1. Introduction

While the first variable speed drives back to the late 1960s, multiphase drives have only gained the special attention of the research community during the past few years in comparison with the traditional three-phase scheme for various applications - especially in those where high reliability and fault tolerance are needed, as cases of ship propulsion, locomotive traction, electric and hybrid electric vehicles, more-electric aircraft,

and high-power industrial applications - and recently in wind energy applications [1]-[3]. Different types of multiphase machines have been recently developed mainly for high-power applications where the increase of the number of phases enables reduction of power per phase, which leads to a reduction of the power per inverter leg. Often the multiphase machines can be classified according to the phase numbers in 5-phase [4]-[8], 6-phase [9]-[11], 9-phase [13]-[14], 12-phase [15]-[17], and 18-phase [18] and by the spatial distribution of the phases within the stator winding symmetrically or asymmetrically. The six-phase induction motor (SpIM) fed by two sets of voltage source inverters was investigated since 1993. Because of the configuration of induction motor having two sets of balanced windings, with phase shift of 30 electrical degrees, six harmonic torque pulsations produced by two sets of windings, respectively, are antiphase and therefore can be completely eliminated. Nowadays, numerous control strategies such as direct torque control (DTC), model-based predictive control (MBPC), and vector control have been developed for SpIM. The DTC technique has the advantages of low machine parameter dependence and fast dynamic torque response. Moreover, the main advantage of the MBPC technique is it focuses on flexibility to define different control criteria, changing only a cost function, a reason why this control technique has been recently applied to the SpIM [19]. MBPC is a control theory developed at the end of the 1970s but has been recently introduced as a viable alternative in power converters and drives. Various control schemes based on MBPC, including current, flux and torque, speed, and sensorless speed control, have been recently reported. Developed schemes have demonstrated good performance in the current and torque control of conventional drives, at the expense of a high computational burden. It is a more flexible control scheme than DTC, and it also provides faster torque response than the field-oriented control (FOC). The interest in predictive control approach and multiphase drives has grown during the last few years, when the development of modern microelectronics devices has removed the computational barriers in their implementation. However, predictive control techniques have been only proved as a viable alternative to conventional controllers in the current regulation of the multiphase power converter. Predictive torque control (PTC), as a variation of the predictive current control methods, has been recently analyzed as an alternative to classic DTC at a theoretical level [20].

In this work, the predictive model of the SpIM is obtained from the vector space decomposition (VSD) approach using the state-space representation method where the two state variables are the stator and rotor currents. As the rotor currents are not measurable parameters, these must be estimated. This chapter hence focuses in the efficiency analysis of the MBPC techniques using the Luenberger Observer (LO) and the optimal estimator based on Kalman Filter (KF). The chapter provides a background material about model-based predictive current control applied to SpIM and includes experimental results by using an experimental setup based on a digital signal controller (DSC). Finally, the main results are discussed in the conclusion section.

2. The SpIM mathematical model

The asymmetrical SpIM with two sets of three-phase stator windings spatially shifted by 30 electrical degrees and isolated neutral points as seen on Figure 1 (a) is one of the most widely discussed topologies. The asymmetrical SpIM is a continuous system which can be described by a set of differential equations. The model can be simplified by using the VSD theory introduced introduced in [21], [22], [26] which enables to transform the

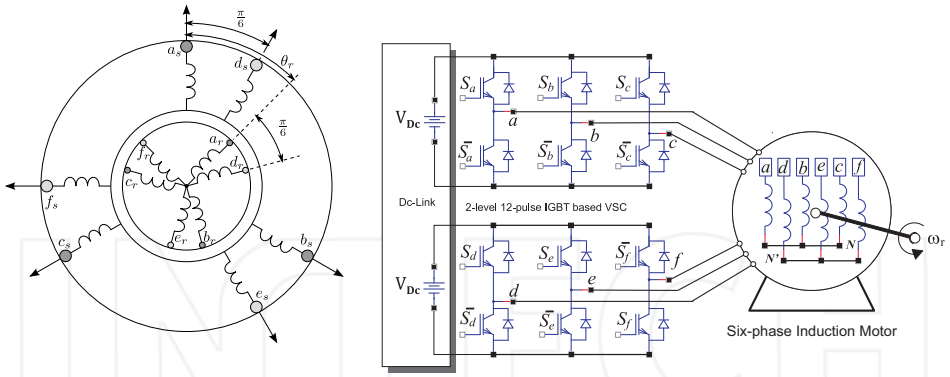

(a) Cross section of an SpIM (b) General scheme of an asymmetrical SpIM drive

Figure 1. Asymmetrical SpIM feed topology and winding configuration

original six-dimensional space of the motor model into three two-dimensional orthogonal subspaces in stationary reference frames $(\alpha-\beta)$, $(x-y)$, and (z_1-z_2) by means of a 6×6 transformation matrix using an amplitude-invariant criterion. This matrix, namely, $\mathbf{T}$, is defined as:

$$\mathbf{T}=\frac{1}{3}\begin{bmatrix} 1 & \frac{\sqrt{3}}{2} & -\frac{1}{2} & -\frac{\sqrt{3}}{2} & -\frac{1}{2} & 0 \\ 0 & \frac{1}{2} & \frac{\sqrt{3}}{2} & \frac{1}{2} & -\frac{\sqrt{3}}{2} & -1 \\ 1 & -\frac{\sqrt{3}}{2} & -\frac{1}{2} & \frac{\sqrt{3}}{2} & -\frac{1}{2} & 0 \\ 0 & \frac{1}{2} & -\frac{\sqrt{3}}{2} & \frac{1}{2} & \frac{\sqrt{3}}{2} & -1 \\ 1 & 0 & 1 & 0 & 1 & 0 \\ 0 & 1 & 0 & 1 & 0 & 1 \end{bmatrix}. \tag{1}$$

It is worth remarking that, according to the VSD approach, the electromechanical energy conversion variables are mapped in the $(\alpha-\beta)$ subspace, meanwhile the current components in the $(x-y)$ subspace represent supply harmonics of order $6n\pm 1$ $(n=1,3,5,...)$ and only produce losses. The voltage vectors in the (z_1-z_2) subspace are zero due to the isolated neutral points configuration [23]. Moreover, the SpIM is supplied by a 2-level 12-pulse IGBT based VSC and a Dc-Link ($\mathbf{V_{Dc}}$), as shown in Figure 1 (b).

The VSC has a discrete nature with a total number of $2^6=64$ different switching state vectors defined by six switching functions corresponding to the six inverter legs $(S_a, S_d, S_b, S_e, S_c, S_f)$, where $S_{a-f}\in\{0,1\}$. The different switching state vectors and the $\mathbf{V_{Dc}}$ voltage define the phase voltages which can in turn be mapped to the $(\alpha-\beta)-(x-y)$ space according to the VSD approach [24]. To represent the stationary reference frame $(\alpha-\beta)$ in the dynamic reference frame $(d-q)$, a rotation transformation can be used. This transformation matrix, namely, $\mathbf{T}_{dq}$ is represented as:

$$\mathbf{T}_{dq} = \begin{bmatrix} cos\,(\theta_r) & sin\,(\theta_r) \\ -sin\,(\theta_r) & cos\,(\theta_r) \end{bmatrix}, \tag{2}$$

where θ_r is the rotor angular position referred to the stator as shown in Figure 1 (a).

From the VSD approach, the following conclusions should be emphasized:

1. The electromechanical energy conversion variables are mapped to the $(\alpha - \beta)$ subspace. Therefore, the fundamental supply component and the supply harmonics of order $12n \pm 1$ $(n = 1, 2, 3, ...)$ are represented in this subspace.
2. The current components in the $(x - y)$ subspace do not contribute to the air-gap flux and are limited only by the stator resistance and stator leakage inductance. These components represent the supply harmonics of the order $6n \pm 1$ $(n = 1, 3, 5, ...)$ and only produce losses, so consequently they should be controlled to be as small as possible.
3. The voltage vectors in the $(z_1 - z_2)$ are zero due to the separated neutral configuration of the machine.

The VSI with isolated neutrals is depicted in Figure 1 (b), being the gating signal represented by $[S_a, ..., S_f]$ and their complementary values by $[\overline{S}_a, ..., \overline{S}_f]$, where $\mathbf{S}_i \in \{0, 1\}$. The discrete nature of the VSI defines the phase voltages which can be mapped in the $(\alpha - \beta) - (x - y)$ according to the VSD approach. Figure 2 shows the active vectors in the $(\alpha - \beta)$ and $(x - y)$ subspaces, where each switching vector state is identified using the switching function by two octal numbers corresponding to the binary numbers $[S_a S_b S_c]$ and $[S_d S_e S_f]$, respectively. Stator voltages are related to the input control signals through the VSI model. An ideal inverter converts gating signals into stator voltages that can be projected to $(\alpha - \beta)$ and $(x - y)$ subspaces and gathered in a row vector $\mathbf{U}_{\alpha\beta xys}$ computed as

$$\mathbf{U}_{\alpha\beta xys} = \left[u_{\alpha s},\, u_{\beta s},\, u_{xs},\, u_{ys},\, 0,\, 0\right]^T = Vdc\,\mathbf{T}\,\mathbf{M}, \tag{3}$$

where $(^T)$ indicates the transposed matrix and $\mathbf{M}$ represents the model of the VSI that can be expressed as function to the switching vectors as follows:

$$\mathbf{M} = \frac{1}{3} \begin{bmatrix} 2 & 0 & -1 & 0 & -1 & 0 \\ 0 & 2 & 0 & -1 & 0 & -1 \\ -1 & 0 & 2 & 0 & -1 & 0 \\ 0 & -1 & 0 & 2 & 0 & -1 \\ -1 & 0 & -1 & 0 & 2 & 0 \\ 0 & -1 & 0 & -1 & 0 & 2 \end{bmatrix} \mathbf{S}^T. \tag{4}$$

As shown in Figure 2, the 64 possible voltage vectors lead to only 49 different vectors in the $(\alpha - \beta)$ and $(x - y)$ subspaces. Applying the transformation matrix, the mathematical model

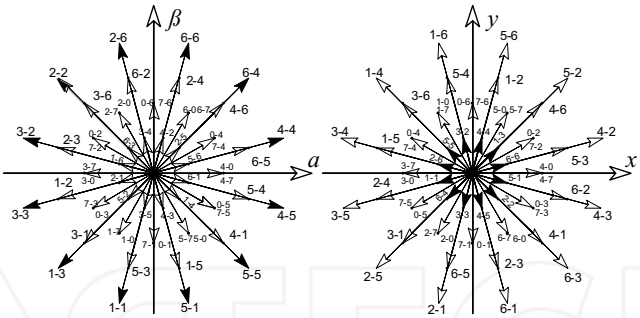

Figure 2. Voltage space vectors and switching states in the $(\alpha - \beta)$ and $(x - y)$ subspaces for a six-phase asymmetrical VSI

of the SpIM can be written using the state-space (SS) representation as follows:

$$[\mathbf{u}]_{\alpha\beta} = [\mathbf{G}]\,\frac{d}{dt}\,[\mathbf{x}]_{\alpha\beta} + [\mathbf{F}]\,[\mathbf{x}]_{\alpha\beta}\,, \tag{5}$$

where $[\mathbf{u}]_{\alpha\beta} = \begin{bmatrix} u_{\alpha s} & u_{\beta s} & 0 & 0 \end{bmatrix}^T$ represents the input vector, $[\mathbf{x}]_{\alpha\beta} = \begin{bmatrix} i_{\alpha s} & i_{\beta s} & i_{\alpha r} & i_{\beta r} \end{bmatrix}^T$ denotes the state vector, and $[\mathbf{F}]$ and $[\mathbf{G}]$ are matrices that define the dynamics of the drive that for the particular case of the SpIM are represented as follows:

$$[\mathbf{F}] = \begin{bmatrix} R_s & 0 & 0 & 0 \\ 0 & R_s & 0 & 0 \\ 0 & \omega_r\, L_m & R_r & \omega_r\, L_r \\ -\omega_r\, L_m & 0 & -\omega_r\, L_r & R_r \end{bmatrix}, \tag{6}$$

$$[\mathbf{G}] = \begin{bmatrix} L_s & 0 & L_m & 0 \\ 0 & L_s & 0 & L_m \\ L_m & 0 & L_r & 0 \\ 0 & L_m & 0 & L_r \end{bmatrix}, \tag{7}$$

where R_s and R_r are the stator and rotor resistance, ω_r is the rotor angular speed, and $L_s = L_{ls} + 3\,L_m$, $L_r = L_{lr} + 3\,L_m$, and L_m are the stator, rotor, and magnetizing inductances, respectively. For a machine with P pairs of poles, the mechanical part of the drive is given by the following equations:

$$T_e = 3\frac{P}{2}\left(\psi_{\beta r} i_{\alpha r} - \psi_{\alpha r} i_{\beta r}\right), \tag{8}$$

$$J_i \frac{d}{dt}\omega_r + B_i \omega_r = \frac{P}{2}\left(T_e - T_L\right), \tag{9}$$

where T_L denotes the load torque, J_i the inertia, $\psi_{\alpha\beta r}$ the rotor flux, and B_i the friction coefficient.

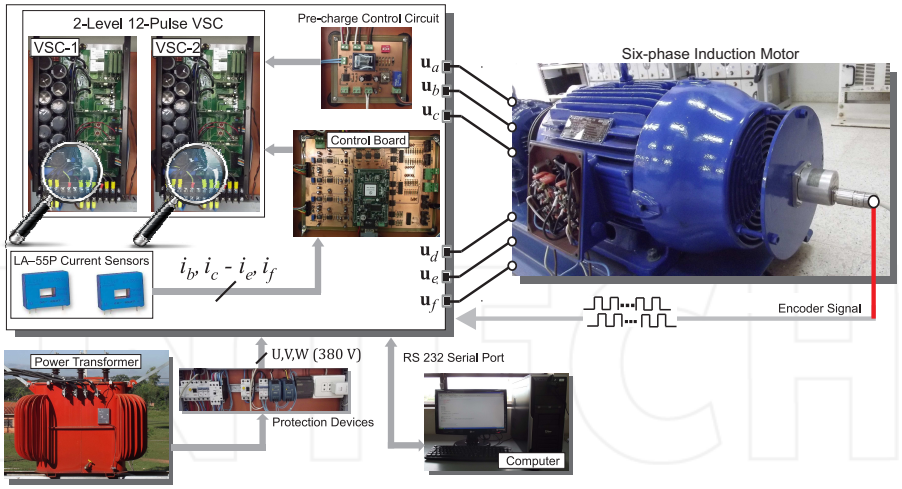

Figure 3. Scheme of the experimental setup

The equations in $(x-y)$ subspace do not link to the rotor side and consequently do not contribute to the air-gap flux; however, they are an important source of Joule losses. Using the SS representation, these equations can be written as:

$$[\mathbf{u}]_{xy} = \begin{bmatrix} L_{ls} & 0 \\ 0 & L_{ls} \end{bmatrix} \frac{d}{dt} [\mathbf{i}]_{xy} + \begin{bmatrix} R_s & 0 \\ 0 & R_s \end{bmatrix} [\mathbf{i}]_{xy}, \tag{10}$$

where L_{ls} represents the stator leakage inductance.

3. SpIM parameter identification

A commercial three-phase induction machine with three pairs of poles, 72 slots, and 15 kW of rated power has been rewound to obtain an asymmetrical six-phase winding (configured with two isolated neutral points) with the same pairs of poles and power with the original three-phase machine. Conventional test (blocked rotor and no-load tests) procedures have been applied to determine experimentally the electrical and mechanical parameters of the SpIM. The obtained values are shown in Table 1.

Two three-phase VSC modules manufactured by Semikron SKS 35F B6U+E1CIF+B6CI21V series are used to generate the six-phase stator voltages and to obtain the experimental results. A hardware timer based on the LM555 device operating in monostable mode is implemented to control the internal pre-charge circuit of both the SKS 35F modules. The Dc-Link voltage is V_{Dc} = 585 V. The implementation of the control system is based on the DSC TMS320LF28335 manufactured by Texas Instruments and the MSK28335 board from Technosoft which has 12 pulse-width modulation (PWM) outputs. The PWM is configured with a 10 kHz of switching frequency. Stator currents are measured by using Hall effect sensors (LA-55P from LEM). The analog-to-digital (A/D) converter peripherals of the MSK28335 board with 16 parallel channels are used to capture all the measured signals. On

	Six-phase induction motor		
Parameter	Symbol	Value	Unit
Stator resistance	R_s	0.62	Ω
Rotor resistance	R_r	0.63	Ω
Stator inductance	L_s	0.2062	H
Rotor inductance	L_r	0.2033	H
Mutual inductance	L_m	0.0666	H
System inertia	J_i	0.27	kg·m^2
Viscous friction coefficient	B_i	0.012	kg·m^2/s
Nominal frequency	f_a	50	Hz
Load torque	T_L	0	N·m
Pair of poles	P	3	–

Table 1. Electrical and mechanical parameters

the other hand, the mechanical speed is measured by employing a Hengstler RI 58-O digital incremental encoder with a resolution of 10,000 pulses per revolution and the enhanced quadrature encoder pulse (eQEP) peripheral of the DSC. To preserve the system integrity, input, and output, digital outputs of the control board are galvanically isolated by means of a Texas Instruments ISO7230CDW isolator. Figure 3 shows a picture of the different parts of the experimental test bench. In order to validate the electrical and mechanical parameters, a PLL software implementation is used to calculate the stator current angle (θ). Finally, the angle is used to calculate the stator current in dynamic reference frame $(i_{ds} - i_{qs})$ using the transformation matrix shown in Eq. (2). Statistical parameters of performance (taking as reference the experimental evolution of stator currents in dynamic reference frame) are quantifiable for two different implementations: the SpIM model based on MatLab/Simulink simulation environment and a real SpIM using the experimental setup.

3.1. Digital PLL implementation

Figure 4 (a) shows that the dynamic performance of the proposed PLL is highly influenced by the compensator G(z). Considering that the reference signal is the stator current in d axis and since the loop gain includes an integral term, θ must track the constant component of the reference signal with zero steady-state error. However, to ensure zero steady-state error, the loop gain must include at least two integrators. Therefore, G(z) must include at least one integral term, that is, one pole at $z = 1$. The other poles and zeros of G(z) are determined mainly by the closed-loop bandwidth requirements of the PLL and stability indices such as phase margin and gain margin, according with the procedure described in [25]. Due to the fact that G(z) is controllable, the transfer function can be expressed into controllable canonical form as follows:

$$\mathbf{x}_{(k+1|k)} = [\mathbf{F}]_{5\times5}\left[\mathbf{x}_{(k|k)}\right]_{5\times1} + [\mathbf{D}]_{5\times1}\left[e_{(k|k)}\right]_{5\times1}, \tag{11}$$

$$\omega^*_{(k|k)} = [\mathbf{C}]_{1\times5}\left[\mathbf{x}_{(k|k)}\right]_{5\times1}, \tag{12}$$

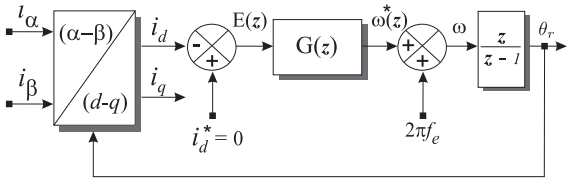

(a) Block diagram of a PLL with special design of the compensator

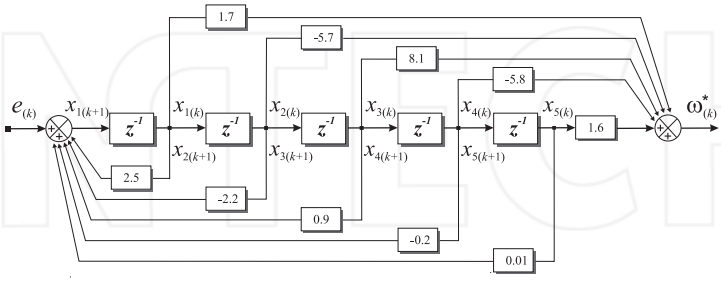

(b) Representation of G(z) transfer function on controllable canonical form

Figure 4. PLL software implementation block diagram

where the matrix $[\mathbf{F}]_{5\times5}$ and the vectors $[\mathbf{D}]_{5\times1}$ and $[\mathbf{C}]_{1\times5}$ define the dynamics of the PLL compensator [G(z)], which for the set of state variables shown in Figure 4 (b) are as follows:

$$[\mathbf{F}]_{5\times5} = \begin{bmatrix} 2.5 & -2.2 & 0.9 & -0.2 & 0.01 \\ 1 & 0 & 0 & 0 & 0 \\ 0 & 1 & 0 & 0 & 0 \\ 0 & 0 & 1 & 0 & 0 \\ 0 & 0 & 0 & 1 & 0 \end{bmatrix}, \tag{13}$$

$$[\mathbf{D}]_{5\times1} = \begin{bmatrix} 1 & 0 & 0 & 0 & 0 \end{bmatrix}^T, \tag{14}$$

$$[\mathbf{C}]_{1\times5} = \begin{bmatrix} 1.7 & -5.7 & 8.1 & -5.8 & 1.6 \end{bmatrix}. \tag{15}$$

This state-space realization is called controllable canonical form because the resulting model is guaranteed to be controllable. Since the control enters a chain of integrators, it has the ability to move every state as shown in Figure 4 (b).

The proposed PLL architecture has been implemented by using the TMS320LF28335 DSC, considering floating-point arithmetic and 10 kHz sampling frequency. The PLL algorithm is executed as an interrupt service routine (ISR), which is triggered by one of the general-purpose timer circuits available on chip. The same timer also triggers the acquisition of input signals, simultaneously with the sampling interrupt. As the on-chip A/D converters have a fast conversion rate (approximately 106-ns conversion time), input data are made available at the beginning of the ISR with negligible time delay. The current components in

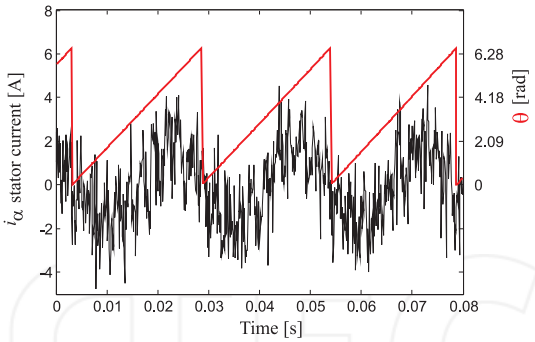

Figure 5. Stator current angle evolution obtained experimentally by using the proposed PLL with special design of the compensator

stationary references frame (α-β) are calculated at each sampling time from the measured phase stator currents ($i_{bs}, i_{cs}, i_{ds}, i_{fs}$) by using Eq. (1), immediately after performing A/D conversion.

Figure 5 shows the stator current angle evolution obtained experimentally by using the proposed PLL architecture, when the SpIM is fed with electrical frequency voltages (f_e) of 40 Hz. It can be seen that the angle evolves from 0 to 2π during a single period of the stator current wave. It is also possible to observe that the result is satisfactory even when the stator currents in stationary reference frame are distorted due to electrical noise.

3.2. SpIM parameter validation

SpIM electrical and mechanical parameters have been analyzed and validated using the experimental setup as well as a SpIM MatLab/Simulink model where a fourth-order Runge-Kutta numerical integration method has been applied to compute the evolution of the state variables step by step in the time domain. Table 1 shows the electrical and mechanical parameters of the asymmetrical SpIM which have been considered during the simulation. The validation of the measured parameters has been evaluated under no-load conditions.

Figure 6 shows the stator current start-up characteristics when a VSC supplied with 585 V of Dc-Link is considered and when a sinusoidal modulation index of 0.275 and 40 Hz of frequency is applied. Figure 6 (a) shows the i_β current evolution of the SpIM provided by the MatLab/Simulink model. In this case, the VSC, the PWM scheme, and the AC motor are simulated within the MatLab/Simulink model. The stator current evolution is compared with the i_d current obtained using the experimental setup in order to verify the analogy between the MatLab/Simulink model simulation results and the experimental results especially with respect to the time constants associated with the SpIM (start-up current, speed, steady-state current, etc.). It can be seen that the time constant converges to the value obtained experimentally both in transient and steady-state conditions where it is possible to quantify a steady-state current of approximately 2 A. Moreover, Figure 6 (b) shows the results obtained experimentally. These results have been compared with the i_d current obtained experimentally. It can be seen that the start-up current evolution converges to a common value for the MatLab/Simulink-based simulations as well as for the experimental

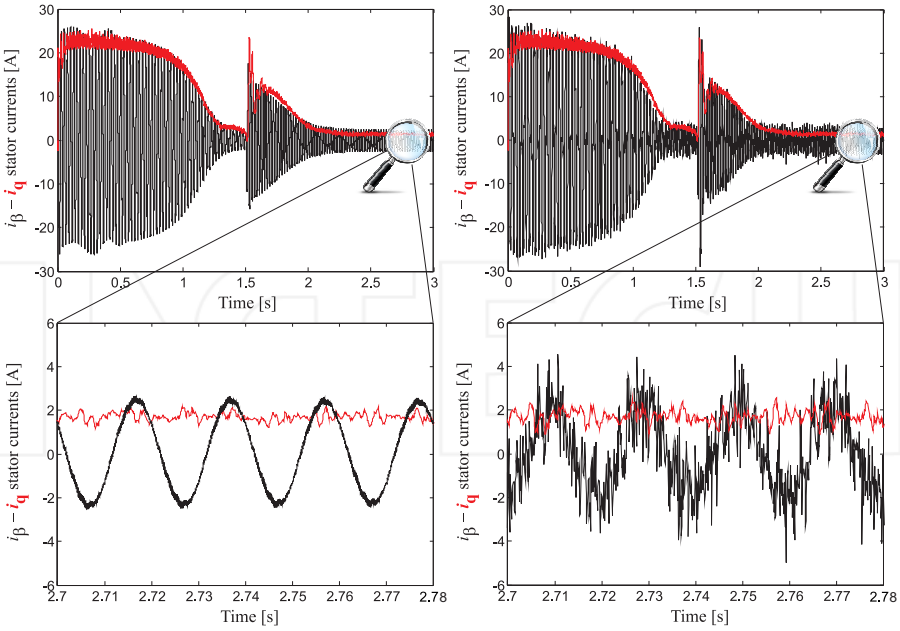

(a) Stator current (i_β) obtained by using the MatLab/Simulink simulation environment

(b) Stator current (i_β) current obtained by experimental tests

Figure 6. Stator current start-up characteristics

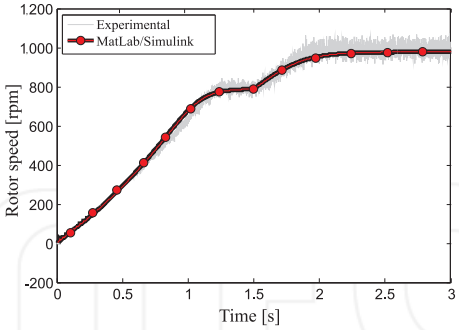

Figure 7. Transient rotor speed evolution

setup, with a start-up transient of approximately 1.15 s. After 1.5 s, the reference frequency is changed from 40 to 50 Hz, while the modulation index is kept constant at 0.275.

Statistical performance parameters such as the covariance, the standard deviation (SD), and the mean square error (MSE) are used in order to evaluate the accuracy of the parameters, taking as reference the results obtained through simulations, as well as those obtained by means of experimental tests. The envelope of the fundamental frequency component of the

	Statistical parameters of performance		
PARAMETER	COVARIANCE	SD	MSE
MatLab/Simulink	1.60×10^{-26}	1.025	1.064
Experimental	5.23×10^{-26}	1.004	1.030

Table 2. Performance analysis.

stator currents in stationary reference frame can be calculated using the Hilbert transform (HT) method. This envelope detection method involves creating the analytic signal of the stator current using the HT. An analytic signal is a complex signal, where the real part ($i_{\alpha s}$) is considered the original signal and the imaginary part ($ji_{\beta s}$) is the HT of the original signal. A discrete-time analytic signal ($\hbar(k)$) can be defined as follows:

$$\hbar(k) = i_{\alpha s}(k) + ji_{\beta s}(k), \tag{16}$$

while the envelope of the signal can be determined by computing the modulus of the analytic signal from the following equation:

$$|\hbar(k)| = \sqrt{\left[\sum_{i=0}^{n} i_{\alpha s}\,(k)\right]^2 + \left[\sum_{i=0}^{n} i_{\beta s}\,(k)\right]^2}. \tag{17}$$

Using the above equation, it is possible to determine the envelope evolution of the stator current, which is used to evaluate those aforementioned statistical performance parameters. This analysis enables to determine the degree of dispersion of the envelope (of the stator current) with respect to the value obtained experimentally through the PLL software implementation (which is shown in red color in Figure 6). The statistic relationship between the curves (i_{qs} and stator current envelope) and the MSE has been analyzed under steady-state conditions. Table 2 details the obtained results for the two different SpIM implementation methods considered in Figure 6. Notice that the obtained performance results are similar for both cases (MatLab/Simulink model and experimental). Moreover, Figure 7 shows the rotor speed evolution for the two cases analyzed before. It can be seen that the results provided by the MatLab/Simulink model in steady state converge to the values obtained experimentally using a motor having three pairs of poles and 50 Hz of nominal frequency (close to 1,000 rpm).

Further analysis has been done to validate the parameters under different test conditions. For example, a change in the modulation index from 0.275 to 0.481 was considered at t = 1.5 s, while a constant voltage frequency of 40 Hz was considered. Figure 8 (a) shows the trajectory of the $i_{\alpha s}$ *vs.* $i_{\beta s}$ as well as ($i_{ds} - i_{qs}$) current evolution considering at least four current periods in steady-state operation, where it is also possible to observe the effect of the change of the modulation index in the reference voltages. Figure 8 (a) shows the results obtained using the MatLab/Simulink model, and Figure 8 (b) shows the experimental results. As in the previous case, it can be seen that the simulated current converges to values equivalent to those obtained experimentally and exhibiting similar dynamic behavior. Finally, Figure 8 (c)

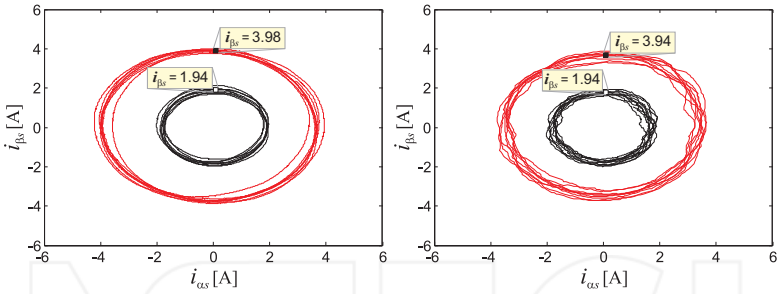

(a) $i_{\alpha s}$ *vs.* $i_{\beta s}$ current obtained by using the MatLab/Simulink simulation environment

(b) $i_{\alpha s}$ *vs.* $i_{\beta s}$ current obtained by experimental tests

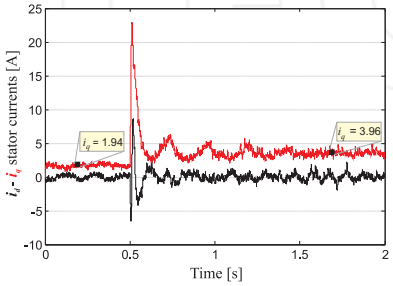

(c) Stator current evolution in dynamic reference frame

Figure 8. Dynamic reference frame characteristics

shows the stator current evolution in the dynamic reference frame $(d-q)$ obtained by means of Eq. (2) using the angle values calculated by the PLL software implementation. It can be seen that the steady-state current values converge to those values shown in **Figure 8 (a)** and Figure 8 (b) before and after applying the change in the modulation index from 0.275 to 0.481, being these values close to 2 and 4 A, respectively. These results validate the SpIM electrical and mechanical parameters shown in Table 1.

4. Predictive model

Assuming the mathematical model expressed by Eq. (5) and using the state variables defined by the vector $[\mathbf{x}]_{\alpha\beta}$, the derivative of states can be defined as follows:

$$\begin{aligned}
\dot{x_1} &= c_3\left(R_r x_3 + \omega_r x_4 L_r + \omega_r x_2 L_m\right) + c_2\left(u_{\alpha s} - R_s x_1\right), \\
\dot{x_2} &= c_3\left(R_r x_4 - \omega_r x_3 L_r - \omega_r x_1 L_m\right) + c_2\left(u_{\beta s} - R_s x_2\right), \\
\dot{x_3} &= c_4\left(-R_r x_3 - \omega_r x_4 L_r - \omega_r x_2 L_m\right) + c_3\left(-u_{\alpha s} + R_s x_1\right), \\
\dot{x_4} &= c_4\left(-R_r x_4 + \omega_r x_3 L_r + \omega_r x_1 L_m\right) + c_3\left(-u_{\beta s} + R_s x_2\right),
\end{aligned} \tag{18}$$

where c_i $(i = 1, 2, 3, 4)$ are constants defined as:

$$c_1 = L_s L_r - L_m^2,\ c_2 = \frac{L_r}{c_1},\ c_3 = \frac{L_m}{c_1},\ c_4 = \frac{L_s}{c_1}. \tag{19}$$

This set of differential equations can be represented in the state-space form as follows:

$$\begin{aligned} \dot{\mathbf{X}}(t) &= f\left(\mathbf{X}(t),\, \mathbf{U}(t)\right), \\ \mathbf{Y}(t) &= \mathbf{C}\mathbf{X}(t), \end{aligned} \tag{20}$$

with state vector $\mathbf{X}(t) = [x_1,\, x_2,\, x_3,\, x_4]^T$, input vector $\mathbf{U}(t) = \left[u_{\alpha s},\, u_{\beta s}\right]$, and output vector $\mathbf{Y}(t) = [x_1,\, x_2]^T$. The components of the vectorial function f and matrix $\mathbf{C}$ are obtained in a straightforward manner from Eq. (18) and the definitions of state and output vector.

The continuous time model represented by Eq. (20) can be discretized in order to be used for the predictive controller using the forward difference approximation method of the first derived, also known as the forward Euler method. Thus, a prediction of the future next-sample state $\hat{\mathbf{X}}(k+1|k)$ is expressed as:

$$\hat{\mathbf{X}}(k+1|k) = \mathbf{X}(k) + T_m f\left(\mathbf{X}(k),\, \mathbf{U}(k)\right), \tag{21}$$

where (k) is the current sample and T_m the sampling time. In Eq. (21), currents and voltages of the stator and the mechanical speed are measurable variables; however, the rotor currents cannot be measured directly. This difficulty can be overcome by means of estimating the rotor current using the reduced-order estimator concept. Figure 9 shows the proposed predictive current control technique for the asymmetrical SpIM.

4.1. The Estimator Based on the State Variables (SV)

The state variables evolution in discrete time can be represented using the following equations:

$$\begin{aligned} \begin{bmatrix} \hat{\mathbf{X}}_a(k+1) \\ \hat{\mathbf{X}}_b(k+1) \end{bmatrix} &= \begin{bmatrix} \overline{\mathbf{A}}_{11} & \overline{\mathbf{A}}_{12} \\ \overline{\mathbf{A}}_{21} & \overline{\mathbf{A}}_{22} \end{bmatrix} \begin{bmatrix} \mathbf{X}_a(k) \\ \mathbf{X}_b(k) \end{bmatrix} + \begin{bmatrix} \overline{\mathbf{B}}_1 \\ \overline{\mathbf{B}}_2 \end{bmatrix} \mathbf{U}_{\alpha\beta s}, \\ \mathbf{Y}(k) &= \begin{bmatrix} \bar{\mathbf{I}}\ \bar{\mathbf{0}} \end{bmatrix} \begin{bmatrix} \mathbf{X}_a(k) \\ \mathbf{X}_b(k) \end{bmatrix}, \end{aligned} \tag{22}$$

where $\mathbf{X}_a = \left[\, i_{\alpha s}(k)\ i_{\beta s}(k) \,\right]^T$ is the vector directly measured which is $\mathbf{Y}$, $\mathbf{X}_b = \left[\, i_{\alpha r}(k)\ i_{\beta r}(k) \,\right]^T$ is the remaining portion to be estimated, $\bar{\mathbf{I}}$ represents the identity matrix, and $\overline{\mathbf{A}}$ and $\overline{\mathbf{B}}$ are matrices whose components are obtained in the following equations:

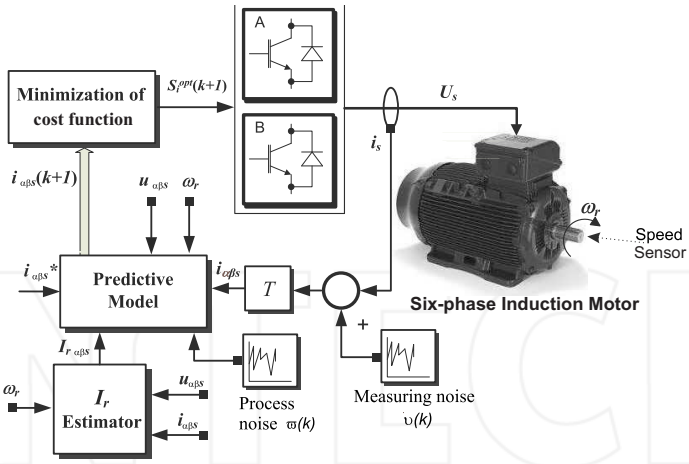

Figure 9. Proposed predictive current control technique for the asymmetrical SpIM

$$\overline{\mathbf{A}} = \begin{bmatrix} (1-T_m c_2 R_s) & T_m c_3 L_m \omega_r & \vdots & T_m c_3 R_r & T_m c_3 L_r \omega_r \\ -T_m c_3 L_m \omega_r & (1-T_m c_2 R_s) & \vdots & -T_m c_3 L_r \omega_r & T_m c_3 R_r \\ \cdots & \cdots & \cdots & \cdots & \cdots \\ T_m c_3 R_s & -T_m c_4 L_m \omega_r & \vdots & (1-T_m c_4 R_r) & -T_m c_4 L_r \omega_r \\ T_m c_4 L_m \omega_r & T_m c_3 R_s & \vdots & T_m c_4 L_r \omega_r & (1-T_m c_4 R_r) \end{bmatrix},$$

$$\overline{\mathbf{B}} = \begin{bmatrix} T_m c_2 & 0 \\ 0 & T_m c_2 \\ \cdots & \cdots \\ -T_m c_3 & 0 \\ 0 & -T_m c_3 \end{bmatrix}. \tag{23}$$

The prediction of the stator currents can be calculated as follows:

$$\hat{i}_{\alpha s}(k+1|k) = (1-T_m c_2 R_s) i_{\alpha s}(k) + T_m c_3 L_m \omega_r(k) i_{\beta s}(k) + T_m c_2 u_{\alpha s}(k) + T_m c_3 \xi_{\alpha s}(k), \tag{24}$$

where $\xi_{\alpha s}(k) = \Big(R_r i_{\alpha r}(k) + L_r \omega_r(k) i_{\beta r}(k)\Big)$.

On the other hand, the quadrature current can be written as follows:

$$\hat{i}_{\beta s}(k+1|k) = -T_m c_3 L_m \omega_r(k) i_{\alpha s}(k) + (1-T_m c_2 R_s) i_{\beta s}(k) + T_m c_2 u_{\beta s}(k) + T_m c_3 \xi_{\beta s}(k), \tag{25}$$

where $\xi_{\beta s}(k) = \Big(R_r i_{\beta r}(k) + L_r \omega_r i_{\alpha r}(k)\Big)$.

It can be seen from the above equations that the prediction of the stator currents has a measurable $(m(k) = \left[m_\alpha(k), m_\beta(k)\right])$ and unmeasured $(e(k) = \left[e_\alpha(k), e_\beta(k)\right])$ parts. Assuming this, the prediction equations can be rewritten as follows:

$$\hat{i}_{\alpha s}(k+1|k) = m_\alpha(k) + e_\alpha(k), \tag{26}$$

$$\hat{i}_{\beta s}(k+1|k) = m_\beta(k) + e_\beta(k), \tag{27}$$

where

$$m_\alpha(k) = (1 - T_m c_2 R_s) i_{\alpha s}(k) + T_m c_3 L_m \omega_r(k) i_{\beta s}(k) + T_m c_2 u_{\alpha s}(k), \tag{28}$$

$$m_\beta(k) = -T_m c_3 L_m \omega_r(k) i_{\alpha s}(k) + (1 - T_m c_2 R_s) i_{\beta s}(k) + T_m c_2 u_{\beta s}(k), \tag{29}$$

$$e_\alpha(k) = T_m c_3 \xi_{\alpha s}(k), \tag{30}$$

$$e_\beta(k) = T_m c_3 \xi_{\beta s}(k). \tag{31}$$

Analyzing Eqs. (26) and (27), which establish a prediction of the stator currents in the $(\alpha - \beta)$ subspace for a $(k+1)$ sampling time using the measurements of the (k) sampling time, it can be noted that the term $m(k)$ contains measurable variables, such as stator currents, rotor speed, and the stator voltages, while the term $e(k)$ contains unmeasurable variables of the asymmetrical SpIM, for this particular case are the rotor currents in the $(\alpha - \beta)$ subspace. Consequently, to solve the equations, it is necessary to obtain an estimate of the value of $\hat{e}(k|k)$, since the rotor currents are not measurable states of the system. This can be solved using the following equations:

$$\hat{e}_\alpha(k|k) = \hat{e}_\alpha(k-1) = i_{\alpha s}(k) - m_\alpha(k-1), \tag{32}$$

$$\hat{e}_\beta(k|k) = \hat{e}_\beta(k-1) = i_{\beta s}(k) - m_\beta(k-1). \tag{33}$$

Considering null initial conditions $\hat{e}_\alpha(0) = 0$ and $\hat{e}_\beta(0) = 0$, the estimated portion that represented the rotor currents can be calculated from a recursive formula given by:

$$\hat{e}_\alpha(k|k) = \hat{e}_\alpha(k-1) + (i_{\alpha s}(k) - \hat{i}_{\alpha s}(k-1)), \tag{34}$$

$$\hat{e}_\beta(k|k) = \hat{e}_\beta(k-1) + (i_{\beta s}(k) - \hat{i}_{\beta s}(k-1)). \tag{35}$$

4.2. The estimator based on a Luenberger Observer

The dynamics of the unmeasured part of the state vector defined by Eq. (22) is described as:

$$\mathbf{X}_b(k+1) = \overline{\mathbf{A}}_{22}\mathbf{X}_b(k) + \overline{\mathbf{A}}_{21}\mathbf{X}_a(k) + \overline{\mathbf{B}}_2\mathbf{U}_{\alpha\beta s}, \tag{36}$$

where the last two terms are known and can be considered as an input for the $\mathbf{X}_b$ dynamics. The $\mathbf{X}_a$ part may be expressed as:

$$\mathbf{X}_a(k+1) - \overline{\mathbf{A}}_{11}\mathbf{X}_a(k) - \overline{\mathbf{B}}_1\mathbf{U}_{\alpha\beta s} = \overline{\mathbf{A}}_{12}\mathbf{X}_b(k). \tag{37}$$

Note that Eq. (37) represents a relationship between a measured quantity on the left and the unknown state vector on the right. Assuming this, Eq. (36) can be rewritten as follows:

$$\begin{aligned}\hat{\mathbf{X}}_b(k+1) = (\overline{\mathbf{A}}_{22} - \mathbf{K}_l\overline{\mathbf{A}}_{12})\hat{\mathbf{X}}_b(k) + \mathbf{K}_l\mathbf{Y}(k+1) + \\ (\overline{\mathbf{A}}_{21} - \mathbf{K}_l\overline{\mathbf{A}}_{11})\mathbf{Y}(k) + (\overline{\mathbf{B}}_2 - \mathbf{K}_l\overline{\mathbf{B}}_1)\mathbf{U}_{\alpha\beta s}(k),\end{aligned} \tag{38}$$

where $\mathbf{K}_l$ is the Luenberger gain matrix. Therefore, Eqs. (37) and (38) describe the dynamics of the reduced-order estimators for Luenberger observer [27].

4.3. The Estimator Based on a Kalman Filter

Considering uncorrelated process and measurement of Gaussian noises, Eq. (22) can be also written as follows:

$$\begin{aligned}\hat{\mathbf{X}}(k+1|k) = \overline{\mathbf{A}}\mathbf{X}(k) + \overline{\mathbf{B}}\mathbf{U}(k) + \mathbf{H}\varpi(k), \\ \mathbf{Y}(k) = \mathbf{C}\mathbf{X}(k) + \nu(k),\end{aligned} \tag{39}$$

where $\mathbf{H}$ is the noise weight matrix, $\varpi(k)$ is the noise matrix of the system model (process noise), and $\nu(k)$ is the matrix noise of measurement. The covariance matrices R_ϖ and R_ν of these noises are defined as:

$$\begin{aligned}R_\varpi = cov(\varpi) = E\left\{\varpi \cdot \varpi^T\right\}, \\ R_\nu = cov(\nu) = E\left\{\nu \cdot \nu^T\right\},\end{aligned} \tag{40}$$

where $E\{.\}$ denotes the expected value. Thus, the dynamics of the reduced-order estimator equations are:

$$\begin{aligned}\hat{\mathbf{X}}_b(k+1|k) = (\overline{\mathbf{A}}_{22} - \mathbf{K}_k\overline{\mathbf{A}}_{12})\hat{\mathbf{X}}_b(k) + \mathbf{K}_k\mathbf{Y}(k+1) + \\ (\overline{\mathbf{A}}_{21} - \mathbf{K}_k\overline{\mathbf{A}}_{11})\mathbf{Y}(k) + (\overline{\mathbf{B}}_2 - \mathbf{K}_k\overline{\mathbf{B}}_1)\mathbf{U}_{\alpha\beta s}(k),\end{aligned} \tag{41}$$

where $\mathbf{K}_k$ represents the KF gain matrix that is calculated at each sampling time in a recursive manner from the covariance of the noises as:

$$\mathbf{K}_k(k) = \mathbf{\Gamma}(k) \cdot \mathbf{C}^T R_\nu^{-1}, \tag{42}$$

where $\mathbf{\Gamma}$ is the covariance of the new estimation, as a function of the old covariance estimation (φ) as follows:

$$\mathbf{\Gamma}(k) = \varphi(k) - \varphi(k) \cdot \mathbf{C}^T (\mathbf{C} \cdot \varphi(k) \cdot \mathbf{C}^T + R_\nu)^{-1} \cdot \mathbf{C} \cdot \varphi(k). \tag{43}$$

From the state equation, which includes the process noise, it is possible to obtain a correction of the covariance of the estimated state as:

$$\varphi(k+1) = \mathbf{A}\mathbf{\Gamma}(k) \cdot \mathbf{A}^T + \mathbf{H} R_\omega \cdot \mathbf{H}^T; \tag{44}$$

this completes the required relations for the optimal state estimation. Thus, $\mathbf{K}_k$ provides the minimum estimation errors, given a knowledge of the process noise magnitude (R_ω), the measurement noise magnitude (R_ν), and the covariance initial condition ($\varphi(0)$) [28].

4.4. Cost function

The cost function should include all aspects to be optimized. In the current predictive control applied to the asymmetrical six-phase induction motor, the most important features to be optimized are the tracking errors of the stator currents in the $(\alpha - \beta)$ subspace for a next sampling time, since these variables are related to the electromechanical conversion. To minimize the prediction errors at each sampling time k, it is enough to utilize a simple term as:

$$J = \| \hat{e}_{i\alpha s}(k+1|k) \|^2 + \| \hat{e}_{i\beta s}(k+1|k) \|^2 \leftrightarrow \begin{cases} \hat{e}_{i\alpha s}(k+1|k) = i^*_{\alpha s}(k+1) - \hat{i}_{\alpha s}(k+1|k), \\ \hat{e}_{i\beta s}(k+1|k) = i^*_{\beta s}(k+1) - \hat{i}_{\beta s}(k+1|k), \end{cases} \tag{45}$$

where $\| \cdot \|$ denotes the vector modulus, i^*_s is a vector containing the reference for the stator currents, and $\hat{i}_s(k+1|k)$ is the prediction of the stator currents calculated from measured and estimated states and the voltage vector $U_{\alpha\beta s}(k)$. Figure 10 (a) shows all projections of the stator current predictions calculated from the prediction model. The current control selects the control vector that minimizes the cost function at each sampling time. Figure 10 (b) shows the selection of the optimal vector based on a minimization of prediction errors.

More complicated cost functions can be devised, for instance, to minimize harmonic content, VSI switching losses, torque and flux, and/or active and reactive power. Also, in multiphase drives, stator current can be decomposed in subspaces in different ways. An appropriate decomposition allows to put more emphasis on harmonic reduction as will be shown in the case study for a six-phase motor drive [29,30]. The most relevant cost functions are shown in Table 3. The superscript $(^*)$ denotes the reference value, and the terms involved in each cost function are detailed in Table 4.

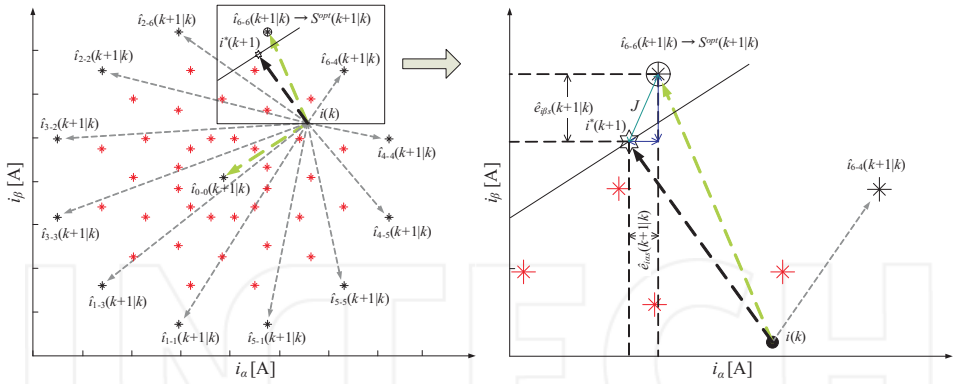

(a) Projection of the stator current prediction in stationary reference frame $(\alpha - \beta)$

(b) Evaluation of the cost function (J) and selection of the optimal vector (S^{opt})

Figure 10. Minimization of tracking error in stator currents in stationary reference frame $(\alpha - \beta)$

Controlled variables	Cost functions (J)
Currents (α-β) and harmonic ($x - y$)	$\|\|i_\alpha^* - i_\alpha\| + \|i_\beta^* - i_\beta\|\|^2 + \lambda\|\|i_x^* - i_x\| + \|i_y^* - i_y\|\|$
Active and reactive power	$\|Q_{in}\| + \|P_{in}^* - P_{in}\|$
Torque and flux	$\|T_e^* - T_e\| + \lambda\|\|\psi_s^*\| - \|\psi_s\|\|$
Currents (α-β) and voltage balance	$\|\|i_\alpha^* - i_\alpha\| + \|i_\beta^* - i_\beta\| + \lambda\|V_{c1} - V_{c2}\|$
Currents (α-β) and VSI switching losses	$\|\|i_\alpha^* - i_\alpha\| + \|i_\beta^* - i_\beta\|\| + \lambda N_s$

Table 3. Possible cost functions in function to the controlled variables

Variable	description
i_α	Measured α current
i_β	Measured β current
i_x	Measured x current
i_y	Measured y current
Q_{in}	Reactive power
P_{in}	Active power
T_e	Torque
ψ_s	Flux of the stator
λ	Weighting factor
V_{c1}, V_{c2}	Voltages on each capacitor (VSI balanced)
N_s	Number of switches

Table 4. Description of the terms involved in each cost function of Table 3

4.5. Optimizer

The optimization is done by exhaustive search over all possible realizations of the control actions. However, for electrical machines, some combinations of gating signals produce the same stator voltages, as shown in Figure 2. This means that, for prediction purposes, they are equivalent. This reduces the effective number of gating combinations to $\varepsilon = 2^\phi - r$, r

being the number of redundant configurations and ϕ the phase numbers of the machine. For the particular case of the SpIM, assuming the previous consideration, the search space for the optimal solution are 49 different vectors (48 active and 1 null). For a generic multiphase machine, the optimization algorithm produces the optimum gating signal combination (S^{opt}) using the estimator based on the state variables as follows:

Algorithm 1 Optimization algorithm for state variable method

$J_o := \infty$, $i := 1$.
while $i \leq \varepsilon$ **do**
  $\mathbf{S}_i \leftarrow \mathbf{S}_{i,j} \; \forall \, j = 1, ..., \phi$.
  comment: Compute stator voltages. Eq. (3).
  comment: Compute the prediction of the states. Eq. (22).
  comment: Compute the cost function. Eq. (45).
  if $J < J_o$ **then**
    $J_o \leftarrow J$, $\mathbf{S}^{opt} \leftarrow \mathbf{S}_i$.
  end if
  $i := i + 1$.
end while

Algorithms 2 and 3 show the pseudocode for the particular case of the proposed estimation methods, the Luenberger observer and Kalman filter, respectively.

Algorithm 2 Proposed algorithm for Luenberger observer method

comment: Optimization algorithm.
$J_o := \infty$, $i := 1$
while $i \leq \varepsilon$ **do**
  $\mathbf{S}_i \leftarrow \mathbf{S}_{i,j} \; \forall \, j = 1, ..., \phi$
  Compute stator voltages. Eq. (3).
  Compute the prediction of the measurement states. Eqs. (36)-(37) assuming null initial conditions $\mathbf{X}_b(0) = 0$.
  Compute the cost function. Eq. (45).
  if $J < J_o$ **then**
    $J_o \leftarrow J$, $\mathbf{S}^{opt} \leftarrow \mathbf{S}_i$
  end if
  $i := i + 1$
end while
Compute the prediction for $\hat{X}_b(k+1)$ by using Eq. (38).

5. Simulation results and discussion

A MatLab/Simulink simulation environment has been designed to analyze the efficiency of the proposed reduced-order observer applied to the model-based predictive current control of the SpIM considering the electrical and mechanical parameters that are shown in Table 1. Numerical integration using fourth-order Runge-Kutta algorithm has been applied to compute the evolution of the state variables step by step in the time domain. A detailed block diagram of the proposed predictive current control technique is provided in Figure 9.

Algorithm 3 Proposed algorithm for Kalman Filter method

Compute the covariance matrix. Eq. (43).
Compute the Kalman Filter gain matrix. Eq. (42).
comment: Optimization algorithm.
$J_o := \infty$, $i := 1$
while $i \leq \varepsilon$ **do**
  $\mathbf{S}_i \leftarrow \mathbf{S}_{i,j} \, \forall \, j = 1, ..., f$
  Compute stator voltages. Eq. (3).
  Compute the prediction of the measurement state. Eq. (39).
  Compute the cost function. Eq. (45).
  if $J < J_o$ **then**
    $J_o \leftarrow J$, $\mathbf{S}^{opt} \leftarrow \mathbf{S}_i$
  end if
  $i := i + 1$
end while
Compute the correction for the covariance matrix. Eq. (44).

The reduced-order observer efficiency has been analyzed by performing parametric simulations considering a 10 kHz of sampling frequency and non-ideal conditions assuming that the control system has measurement (R_v) and process (R_w) noises. Figure 11 (a) (top) shows the obtained parametric simulation results for the particular case of the estimator based on the SV technique when are considered a constant frequency reference of 50 Hz with 15 A of reference current in stationary reference frame ($i_{\alpha s}$) and different levels of measurement and process noises (from 0 to 0.16) under varying load torque conditions (from 0 to 20 N·m). It can be seen in this figure the evolution of the MSE (measured between the reference and simulated currents) when the load torque and the measurement and process noises simultaneously increase. This behavior is associated with uncertainties in the estimation of the stator current due to the method based on the state variables. It can be observed that the MSE increases in direct proportion under varying load torque conditions (from 0.25 to 0.65 A). Figure 11 (a) (middle) shows the stator current tracking characteristic, where the following parameters are considered: $R_v = R_w$ = 0.08 and T_L = 10 N·m. The references and simulated and prediction currents are represented in red, black, and green colors, respectively. According to Table 5, under these operating conditions, the performance of the MBPC based on the SV method in terms of MSE$i_{\alpha s}$ and THD$i_{\alpha s}$ can be quantified in 0.69 A and 6 %, respectively. On the other hand, Figure 11 (a) (bottom) shows the rotor current evolution, calculated according to the SV methods under the same conditions described above.

Moreover, Figure 11 (b) (top) and Figure 11 (c) (top) show the parametric simulation of the MBPC technique for cases based on the LO and KF estimators, respectively. It can be noted in these graphs that the proposed MBPC methods based on the LO and KF estimators introduce improvements quantified with respect to the MSE, mainly when these control algorithms are compared with the MBPC method based on state variables. It can be concluded from these graphs that the MBPC based on the LO and KF estimators exhibits low sensitivity (in terms of MSE) to change of the load torque, and the performance is related with the measurement and process noise levels. Under the same test conditions considered above, the MSE measured between the reference and simulated currents in alpha axis are 0.47 A and 0.48 A for

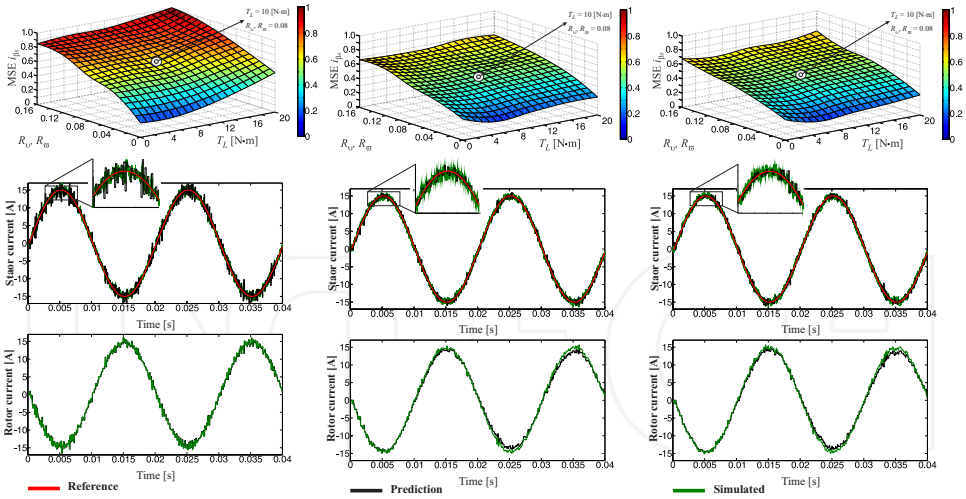

(a) Estimator based on the SV (b) Estimator based on the LO (c) Estimator based on the KF

Figure 11. Performance analysis considering a 15 A and 50 Hz of reference current

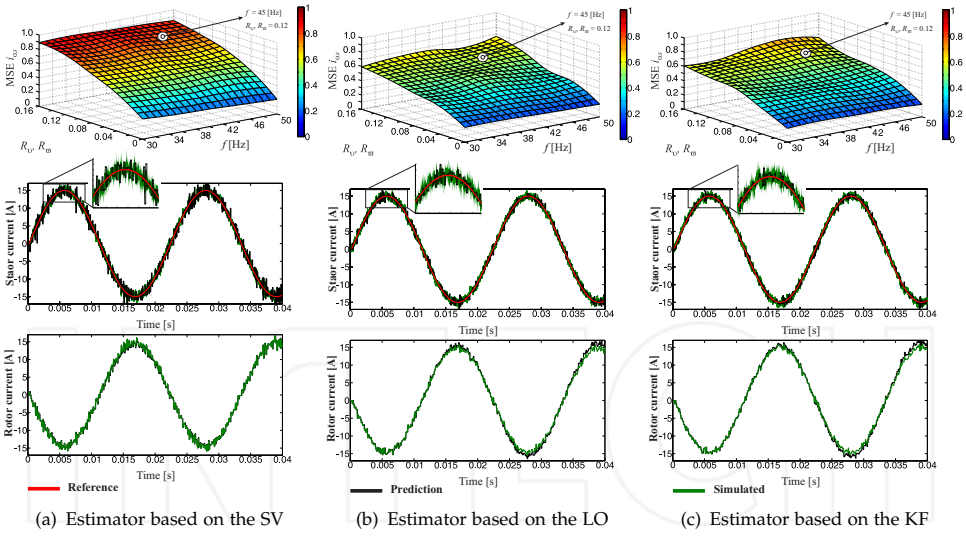

(a) Estimator based on the SV (b) Estimator based on the LO (c) Estimator based on the KF

Figure 12. Performance analysis considering a 15 A of reference current and $T_L = 0$

Figure 11 (b) (middle) and Figure 11 (c) (middle), respectively. Figure 11 (b) (bottom) and Figure 11 (c) (bottom) show the rotor current estimated, for the cases based on the LO and KF estimators, respectively.

The performance of the MBPC based on reduced-order estimators has been evaluated considering a 15 A of reference current with no-load condition and different levels of measurement and process noises (from 0 to 0.16) under varying reference frequencies (from 30 to 50 Hz). Figure 12 (top) shows the performance analysis in terms of MSE, where it is possible to observe from the parametric simulation that the three control methods evaluated has low sensitivity to the frequency variation when are considered no-load conditions. It can be seen that the efficiency strongly depends on the measurement and process noise levels, as in the previous case. Figure 12 (middle) shows the stator current tracking characteristic, where the following parameters are considered: $R_v = R_w$ = 0.12 and 45 Hz of reference frequency. Finally, Figure 12 (bottom) shows the rotor current estimated, for the case of study.

	Figure 11 analysis			
	MSE$i_{\alpha s}$	MSE$i_{\beta s}$	THD$i_{\alpha s}$	THD$i_{\beta s}$
State variables	0.6965	0.6571	6.00%	6.06%
Luenberger observer	0.4799	0.4971	4.39%	4.62%
Kalman filter	0.4802	0.5084	4.29%	4.37%
	Figure 12 analysis			
	MSE$i_{\alpha s}$	MSE$i_{\beta s}$	THD$i_{\alpha s}$	THD$i_{\beta s}$
State variables	0.7798	0.7702	7.44%	7.17%
Luenberger observer	0.5622	0.5951	5.13%	5.18%
Kalman filter	0.5897	0.5208	5.10%	5.20%

Table 5. Performance analysis

A similar analysis was performed for the case of beta current component, obtaining similar results as shown in Table 5. These simulation results substantiate the expected performance of the proposed algorithms based on reduced-order observers.

6. Conclusion

In this chapter, an efficiency analysis of two reduced-order observers for rotor current estimator applied to the model-based predictive current control of the SpIM has been presented. The electrical and mechanical parameters of the SpIM have been measured and validated experimentally using an experimental setup. Real 15 kW SpIM parameters have been used to perform simulations using a MatLab/Simulink simulation environment. The simulation results obtained by different operation points under no-load and full-load conditions as well as different measurement and process noises have shown an increase in the efficiency of the proposed current control methods (based on the Kalman filter and Luenberger observer) measured with respect to the mean squared error of the stator currents in stationary reference frame, especially when they are compared with the control method based on state variables. Furthermore, the optimal estimator based on the Kalman filter achieves better performance than the Luenberger observer in terms of THD, mainly because it takes into account the effects of the noises in the control structure, recalculating the state feedback matrix at each sampling time recursively given the covariance of the new estimation

as a function of the old covariance estimation. These results show that the experimental implementation of these control techniques are feasible and can be applied to the SpIM to increase the efficiency of the MBPC technique.

Acknowledgment

The authors would like to thank the Paraguayan Government for the economical support they provided by means of a CONACYT grant project 14-INV-101 – Desarrollo y análisis de eficiencia de nuevos algoritmos de control enfocados al generador hexafásico en aplicaciones de energía eólica. In addition, they wish to express their gratitude to the reviewers for their helpful comments and suggestions.

Author details

Raúl Gregor[1*], Jorge Rodas[1], Derlis Gregor[2] and Federico Barrero[3]

*Address all correspondence to: gregor.raul@gmail.com

1 Facultad de Ingeniería, Universidad Nacional de Asuncion, Department of Power and Control Systems, Asuncion, Paraguay

2 Facultad de Ingeniería, Universidad Nacional de Asuncion, Department of Computer Science, Asuncion, Paraguay

3 Escuela Superior de Ingenieros, Universidad de Sevilla, Department of Electronic Engineering, Sevilla, España

References

[1] E. Levi, "Multiphase Electric Machines for Variable-Speed Applications", Industrial Electronics, IEEE Transactions on, vol. 55, no. 5, pp. 1893–1909, 2008.

[2] H. Guzman, M.J. Duran, F. Barrero, B. Bogado, and S. Toral, "Speed Control of Five-Phase Induction Motors With Integrated Open-Phase Fault Operation Using Model-Based Predictive Current Control Techniques", Industrial Electronics, IEEE Transactions on, vol. 61, no. 9, pp. 4474–4484, 2014.

[3] H.S. Che, M.J. Duran, E. Levi, M. Jones, W.P. Hew, and N.A. Rahim, "Postfault Operation of an Asymmetrical Six-Phase Induction Machine With Single and Two Isolated Neutral Points", Power Electronics, IEEE Transactions on, vol. 29, no. 10, pp. 5406–5416, 2014.

[4] M. Salehifar, R. Salehi Arashloo, M. Moreno-Eguilaz, V. Sala, and L. Romeral, "Observer-Based Open Transistor Fault Diagnosis and Fault-Tolerant Control of Five-Phase Permanent Magnet Motor Drive for Application in Electric Vehicles", Power Electronics, IET, vol. 8, no. 1, pp. 76–87, 2015.

[5] Y. Zhao, H. Wang, and L. Xiao, "Investigation of Fault-Tolerant Capability of Five-Phase Doubly Salient Electromagnetic Generator", Electric Power Applications, IET, vol. 9, no. 1, pp. 80–93, 2015.

[6] A. Mohammadpour, and L. Parsa, "Global Fault-Tolerant Control Technique for Multiphase Permanent-Magnet Machines", Industry Applications, IEEE Transactions on, vol. 51, no. 1, pp. 178–186, Jan.–Feb. 2015.

[7] A.S. Abdel-Khalik, S. Ahmed, A.A. Elserougi, and A.M. Massoud, "Effect of Stator Winding Connection of Five-Phase Induction Machines on Torque Ripples Under Open Line Condition", Mechatronics, IEEE/ASME Transactions on, vol. 20, no. 2, pp. 580–593, Apr. 2015.

[8] H. Guzman, F. Barrero, and M.J. Duran, "IGBT-Gating Failure Effect on a Fault-Tolerant Predictive Current-Controlled Five-Phase Induction Motor Drive", Industrial Electronics, IEEE Transactions on, vol. 62, no. 1, pp. 15–20, Jan. 2015.

[9] S.M.J. Rastegar Fatemi, N.R. Abjadi, J. Soltani, and S. Abazari, "Speed sensorless control of a six-phase induction motor drive using backstepping control", Power Electronics, IET, vol. 7, no. 1, pp. 114–123, Jan. 2014.

[10] H. Yashan, Z. Zi-Qiang, and L. Kan, "Current Control for Dual Three-Phase Permanent Magnet Synchronous Motors Accounting for Current Unbalance and Harmonics", Emerging and Selected Topics in Power Electronics, IEEE Journal of, vol. 2, no. 2, pp. 272–284, Jun. 2014.

[11] H.S. Che, E. Levi, M. Jones, H. Wooi-Ping, and N.A. Rahim, "Current Control Methods for an Asymmetrical Six-Phase Induction Motor Drive", Power Electronics, IEEE Transactions on, vol. 29, no. 1, pp. 407–417, Jan. 2014.

[12] L. Feng, H. Wei, C. Ming, and Z. Gan, "Analysis of Fault Tolerant Control for a Nine-Phase Flux-Switching Permanent Magnet Machine", Magnetics, IEEE Transactions on, vol. 50, no. 11, pp. 1–4, Nov. 2014.

[13] E. Jung, Y. Hyunjae, S. Seung-Ki, C. Hong-Soon, and C. Yun-Young, "A Nine-Phase Permanent-Magnet Motor Drive System for an Ultrahigh-Speed Elevator", Industry Applications, IEEE Transactions on, vol. 48, no. 3, pp. 987–995, May.–Jun. 2012.

[14] M. Ruba, and D. Fodorean, "Analysis of Fault-Tolerant Multiphase Power Converter for a Nine-Phase Permanent Magnet Synchronous Machine", Industry Applications, IEEE Transactions on, vol. 48, no. 6, pp. 2092–2101, Nov.–Dec. 2012.

[15] O. Bottauscio, G. Serra, M. Zucca, and M. Chiampi, "Role of Magnetic Materials in a Novel Electrical Motogenerator for the More Electric Aircraft", Magnetics, IEEE Transactions on, vol. 50, no. 4, pp. 1–4, Apr. 2014.

[16] J.M. Apsley, and S. Williamson, "Analysis of Multiphase Induction Machines with Winding Faults", Industry Applications, IEEE Transactions on, vol. 42, no. 2, pp. 465–472, Mar.–Apr. 2006.

[17] J.M. Apsley, S. Williamson, A.C. Smith, and M. Barnes, "Induction Motor Performance as a Function of Phase Number", Electric Power Applications, IEE Proceedings, vol. 153, no. 6, pp. 898–904, Nov. 2006.

[18] O. Grigore-Muler, and M. Barbelian, "The Simulation of a Multi-Phase Induction Motor Drive", Optimization of Electrical and Electronic Equipment (OPTIM), 2010 12th International Conference on, pp. 297–306, 20–22 May. 2010.

[19] Y. Hu, Z.Q. Zhu, and K. Liu, "Current Control for Dual Three-Phase Permanent Magnet Synchronous Motors Accounting for Current Unbalance and Harmonics", Emerging and Selected Topics in Power Electronics, IEEE Journal of, vol. 2, no. 2, pp. 272–284, 2014.

[20] J.A. Riveros, F. Barrero, E. Levi, M.J. Duran, S. Toral, and M. Jones, "Variable-Speed Five-Phase Induction Motor Drive Based on Predictive Torque Control", Industrial Electronics, IEEE Transactions on, vol. 60, no. 8, pp. 2957–2968, Aug. 2013.

[21] H.S. Che, E. Levi, M. Jones, M. Duran, W.P. Hew, and N. Abd Rahim, "Operation of a Six-Phase Induction Machine Using Series-Connected Machine-Side Converters", Industrial Electronics, IEEE Transactions on, vol. 61, no. 1, pp. 164–176, Jan. 2014.

[22] Y. Zhao and T. Lipo, "Space Vector PWM Control of Dual Three-Phase Induction Machine Using Vector Space Decomposition", Industry Applications, IEEE Transactions on, vol. 31, no. 5, pp. 1100–1109, Sep. 1995.

[23] H.S. Che, M. Duran, E. Levi, M. Jones, W.P. Hew, and N. Abd Rahim, "Postfault Operation of an Asymmetrical Six-Phase Induction Machine with Single and Two Isolated Neutral Points", Power Electronics, IEEE Transactions on, vol. 29, no. 10, pp. 5406–5416, Oct. 2014.

[24] F. Barrero, J. Prieto, E. Levi, R. Gregor, S. Toral, M. Duran, and M. Jones, "An Enhanced Predictive Current Control Method for Asymmetrical Six-Phase Motor Drives", Industrial Electronics, IEEE Transactions on, vol. 58, no. 8, pp. 3242–3252, Aug. 2011.

[25] A. Yazdani and R. Iravani, "Voltage-Sourced Converters in Power Systems: Modeling, Control, and Applications", New Jersey, USA: Wiley, 2010, pp. 213–216.

[26] F. Barrero, M.R. Arahal, R. Gregor, S. Toral, and M.J. Duran, "A Proof of Concept Study of Predictive Current Control for VSI-Driven Asymmetrical Dual Three-Phase AC Machines", Industrial Electronics, IEEE Transactions on, vol. 56, no. 6, pp. 1937–1954, Jun. 2009.

[27] M. Arahal, F. Barrero, S. Toral, M.J. Duran, and R. Gregor, "Multi-phase Current Control Using Finite-State Model-Predictive Control", Control Engineering Practice, vol. 17, no. 5, pp. 579–587, Oct. 2008.

[28] R. Vargas, P. Cortes, U. Ammann, J. Rodriguez, and J. Pontt, "Predictive Control of a Three-Phase Neutral-Point-Clamped Inverter", Industrial Electronics, Transactions on, vol. 54, no. 5, pp. 2697–2705, Oct. 2007.

INTECH